Received: 18 May 2021 | Revised: 24 September 2021 | Accepted: 27 September 2021

DOI: 10.1002/mrm.29045

RESEARCH ARTICLE

Magnetic Resonance in Medicine

Enhancing the spatial resolution of hyperpolarized carbon-13 MRI of human brain metabolism using structure guidance

Matthias J. Ehrhardt[1,2] | **Ferdia A. Gallagher**[3] | **Mary A. McLean**[3,4] | **Carola-Bibiane Schönlieb**[5]

[1]Department of Mathematical Sciences, University of Bath, Bath, UK

[2]Institute for Mathematical Innovation, University of Bath, Bath, UK

[3]Department of Radiology, University of Cambridge, Cambridge, UK

[4]Cancer Research UK Cambridge Institute, University of Cambridge, Cambridge, UK

[5]Department for Applied Mathematics and Theoretical Physics, University of Cambridge, Cambridge, UK

Correspondence
Matthias J. Ehrhardt, Institute for Mathematical Innovation, University of Bath, Bath, UK.
Email: m.ehrhardt@bath.ac.uk

Funding information
Mark Foundation Institute for Cancer Research; Leverhulme Trust, Grant/Award Number: ECF-2019-478 and Philip Leverhulme Prize; Wellcome Trust, Grant/Award Number: RG98755; Royal Society, Grant/Award Number: Wolfson Fellowship; Cambridge Experimental Cancer Medicine Centre; Alan Turing Institute; Cantab Capital Institute for the Mathematics of Information; H2020 European Research Council, Grant/Award Number: 777826; National Institute for Health Research, Grant/Award Number: Cambridge Biomedical Research Centre; Cancer Research UK, Grant/Award Number: C19212/A16628, C19212/A911376, C19212/A27150 and C968; Engineering and Physical Sciences Research Council, Grant/Award Number: EP/S026045/1, EP/T026693/1, EP/T007745/1 and EP/T0035

Purpose: Dynamic nuclear polarization is an emerging imaging method that allows noninvasive investigation of tissue metabolism. However, the relatively low metabolic spatial resolution that can be achieved limits some applications, and improving this resolution could have important implications for the technique.

Methods: We propose to enhance the 3D resolution of carbon-13 magnetic resonance imaging (^{13}C-MRI) using the structural information provided by hydrogen-1 MRI (^{1}H-MRI). The proposed approach relies on variational regularization in 3D with a directional total variation regularizer, resulting in a convex optimization problem which is robust with respect to the parameters and can efficiently be solved by many standard optimization algorithms. Validation was carried out using an in silico phantom, an in vitro phantom and in vivo data from four human volunteers.

Results: The clinical data used in this study were upsampled by a factor of 4 in-plane and by a factor of 15 out-of-plane, thereby revealing occult information. A key finding is that 3D super-resolution shows superior performance compared to several 2D super-resolution approaches: for example, for the in silico data, the mean-squared-error was reduced by around 40% and for all data produced increased anatomical definition of the metabolic imaging.

Conclusion: The proposed approach generates images with enhanced anatomical resolution while largely preserving the quantitative measurements of metabolism. Although the work requires clinical validation against tissue measures of metabolism, it offers great potential in the field of ^{13}C-MRI and could significantly improve image quality in the future.

KEYWORDS
human brain, hyperpolarized ^{13}C, magnetic resonance imaging, super-resolution, variational regularization

1 | INTRODUCTION

Dynamic nuclear polarization is an emerging method to noninvasively probe tissue metabolism, which has recently been translated into patient imaging.[1] The method transiently increases the sensitivity of Carbon-13 Magnetic Resonance Imaging (^{13}C-MRI) experiments by over 10,000-fold,[2] which enables the metabolism of an injected ^{13}C-labeled precursor molecules to be investigated dynamically, for example, observing the conversion of hyperpolarized [1-^{13}C]pyruvate to [1-^{13}C]lactate in vivo in humans.[3] This reaction, catalyzed by the enzyme lactate dehydrogenase (LDH) has many promising applications in oncology, where it can be used to characterize tumors and assess response to therapy.[4] We have recently demonstrated its role in studying metabolism in the healthy human brain following rapid transport of the [1-^{13}C]pyruvate across the intact blood-brain barrier,[5] opening up the possibility of applying the technique in a range of neurological disorders where metabolism is altered.[6]

However, even with the large enhancement in sensitivity that can be achieved, the spatial resolution attained is significantly lower than can be acquired with conventional proton MRI (^{1}H-MRI) and also lower than the resolution achievable with comparable clinical metabolic techniques such as positron emission tomography (PET). Although a bolus of up to 10 mmol of hyperpolarized labeled pyruvate is rapidly injected intravenously into the patient, the tissue concentration is only ∼0.1 mM due to dilution in the vascular and extravascular spaces,[7] which is dwarfed in comparison to the endogenous concentration of hydrogen atoms in tissue. Given the transient nature of the hyperpolarized signal, which decays with a time constant (T_1) of ∼25–30 s in vivo, rapid single-shot techniques for imaging the ^{13}C signal are frequently employed to characterize the dynamic nature of the signal. The resulting pixel dimensions are in the order of 1 cm in plane, with a slice thickness which is often larger and compares unfavorably with the 1 mm isotropic resolution routinely achieved with conventional ^{1}H-MRI. This significant difference in image scale greatly limits the ability to discriminate small areas of metabolic variability, and interpretation relies on co-registering the metabolic maps with the corresponding morphology on the ^{1}H-MRI. In the brain, differences in ^{13}C-pyruvate metabolism have been demonstrated between and within both the gray and white matter.[5,8] However, the resolution of this metabolic heterogeneity is limited due to partial volume effects when each image pixel contains signal from a mixture of cell and tissues. Therefore we investigated whether mathematical techniques for 3D super-resolution can help bridge this divide by using structural information on the higher resolution ^{1}H-MRI to enhance the lower resolution metabolic imaging.

Super-resolution methods have been applied to a range of medical imaging techniques such as PET,[9–11] diffusion-weighted MRI,[12] spectroscopic imaging,[13,14] ^{23}Na-MRI,[15] ^{19}F-MRI,[16] T_1/T_2weighted MRI,[17–20] fMRI[21] and recently also to ^{13}C-MRI[22–24] which is the setting of this paper. Several approaches have been taken to enhance the resolution of ^{1}H-MRI including in the k-space dimension (e.g., Refs. [18, 19, 21]) as well as in the image space (e.g., Refs. [17, 20]). Image space-based approaches are usually easier to implement and computationally more efficient. Here we apply an image-based super-resolution approach in the setting of a low-resolution metabolic image (termed *data*) and a high-resolution anatomical image (termed *guide*), with a new image being computed which has the contrast of the data and the spatial resolution of the guide, see also Figure 1. Image super-resolution is often undertaken using *variational regularization*, that is, by solving

$$\min_x \|Sx - y\|^2 + \alpha \mathscr{R}(x), \tag{1}$$

where S models the loss in resolution moving from high to low and $\mathscr{R}$ encapsulates possible a priori information about the super-resolved image, such as being *similar* to the guide. The regularization parameter α allows to trade-off these two terms, thus reconstructing images which explain the data but also resemble the prior information to a certain extent. For an overview of the state-of-the-art in variational regularization with structural guidance, see Ref. [25].

In this paper, we investigate the use of super-resolution of ^{13}C-MRI with the aid of a ^{1}H-MRI guide, thereby potentially overcoming the current limitations of ^{13}C-MRI, see Figure 1 for a graphical illustration of this idea. We show that the commonly used 2D approach is not sufficient to reconstruct biologically well-defined images and an extension to three spatial dimensions is needed; see Figure 2 for an illustration. By using variational regularization in 3D with a directional total variation regularizer, we show that the enhanced images have a significant improvement in resolution compared

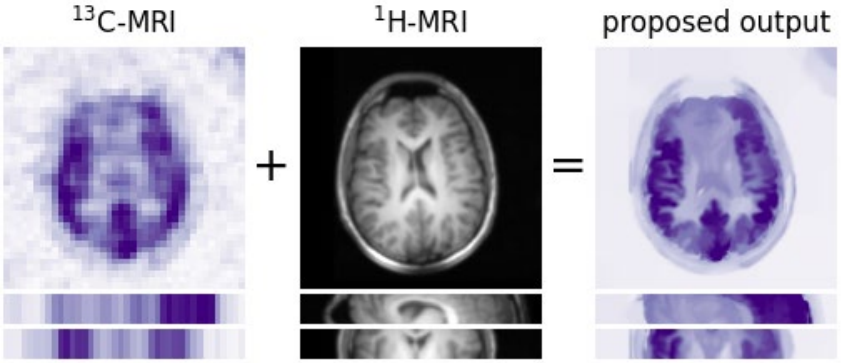

FIGURE 1 Concept of the approach taken in the paper: Use 3D structural information of ^{1}H-MRI (*guide*) to improve the resolution of ^{13}C-MRI (*data*). In this figure and in subsequent figures, we visualize 3D data by displaying three slices in the axial, sagittal and coronal orientations (from top to bottom)

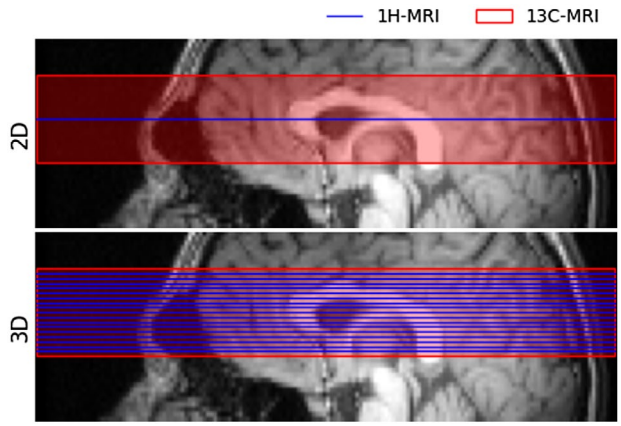

FIGURE 2 Data used in the proposed method: Instead of taking a single ^{1}H-MRI slice to upsample the ^{13}C-MRI data, we propose using a stack of slices covering the whole ^{13}C-MRI field-of-view

to the original unprocessed data and compare favorably to other previously applied super-resolution approaches. This is the first time that a planar image is super-resolved using volumetric information, which not only unlocks the potential of ^{13}C-MRI but a similar approach will be beneficial to many other imaging modalities where spatial resolution is the limiting factor.

2 | THEORY

2.1 | Inverse problem

We approach the problem of super-resolution as an inverse problem where we aim to solve a linear equation

$$Sx = y \tag{2}$$

where x is the high-resolution image to be reconstructed, y is the measured data and S models the loss in resolution. For the proposed approach $x \in \mathbb{R}^{M\times N\times K}$ is 3D and $y \in \mathbb{R}^{m\times n}$ 2D. For simplicity, let $M = N = sm = sn$ for a fixed super-resolution factor $s \in \mathbb{N}$. Then the used resolution model S can be defined via

$$(Sx)_{i,j} = \sum_{k=1}^{K} \sum_{a=0}^{s-1} \sum_{b=0}^{s-1} x_{i+a,j+b,k} \tag{3}$$

for $i \in \{1, \dots, m\}$ and $j \in \{1, \dots, n\}$. Since S has a large kernel, a priori information, for example, via variational regularization (1) must be included to solve the inverse problem (2). Here we approach this by including a priori structural guide information into the regularizer $\mathscr{R}$.

2.2 | Structure-guided regularization

A popular regularizer for variational regularization (1) is the total variation which can be defined as

$$\mathrm{TV}(x) = \sum_{\beta} \|(\nabla x)_\beta\| \tag{4}$$

where $\nabla x \in \mathbb{R}^{M\times N\times K\times 3}$ is a finite-difference approximation of the *gradient* of x, see Ref. [26] for formulas in 2D which are easy to extend to 3D and $\beta = (\beta_1, \beta_2, \beta_3) \in \mathbb{N}^3$ is a multi-index. While the total variation has many benefits such as preserving edges, it is impossible to include structural a priori information from a guide in its native formulation (4) and a generalized formulation is required.

The mathematical modeling of structural guide information has significantly advanced over the last decade (see Ref. [25] for an overview). Most successful approaches are based on the idea that two images x and v are *structurally similar* if they have colinear (or parallel) gradients, that is, for any location β with non-vanishing gradients, there exists a $\lambda \in \mathbb{R}$ such that

$$(\nabla x)_\beta = \lambda(\nabla v)_\beta. \tag{5}$$

Many regularizers can encode such information, for example, total nuclear variation, joint total variation, see Ref. [25] for more information. A simple yet powerful way to include

such structural information is the directional total variation,[19] defined as

$$\mathrm{dTV}(x) = \sum_{\beta} \|D_\beta (\nabla x)_\beta\| \tag{6}$$

with $D_\beta = I - \gamma \xi_\beta \xi_\beta^T \in \mathbb{R}^{3\times 3}$ and

$$\xi_\beta = \frac{(\nabla v)_\beta}{\sqrt{\|(\nabla v)_\beta\|^2 + \eta^2}} \in \mathbb{R}^3. \tag{7}$$

It is important to note that the directional total variation does not depend directly on the intensities of the guide v but rather the location and direction of its edges via ξ, see Figure 3. Both γ and η can be tuned to maximize performance but $\gamma = 0.9995$ and $\eta = 10^{-2}\max_\beta \|(\nabla v)_\beta\|$ have been shown to be good default options for many applications, cf. for example.[19,27]

2.3 | Algorithm

Problem (1) can be written as

$$\min_x f(Ax) + g(x) \tag{8}$$

for f, g which are proper, convex, and lower semicontinuous (but not necessarily smooth) and a matrix A. When f or g are nonsmooth ($\mathscr{R} = \mathrm{dTV}$), then (8) used to be a challenging problem, but there are many algorithms to solve it nowadays, see Ref. [28] for an overview. We use a popular algorithm called primal-dual hybrid gradient (PDHG) which is also known in the literature as the Chambolle–Pock algorithm.[26] To solve (1) with directional total variation, we choose $g \equiv 0$, $A = (S;D)$, $f(u_1, u_2) = \|u_1 - y\|^2 + \alpha\|u_2\|_1$, which can be easily implemented in Operator Discretization Library (ODL).[29] The python code and data can be accessed on https://zenodo.org/badge/latestdoi/417512547.

3 | METHODS

We validate the proposed approach and compare it to its 2D variant on one in silico phantom, an in vitro phantom, and in vivo data from four human volunteers, see Figure 4 for a graphical overview of the data. Local ethical approval was obtained for the acquisition of human data (NRES Committee East of England, Cambridge South, REC number 15/EE/0255).

3.1 | Datasets

3.1.1 | In vitro phantom

Phantom experiments were similar to those previously published in Ref. [30]. Imaging phantoms consisted of 15 ml Falcon tubes filled to 14 ml with five times concentrated phosphate-buffered saline at pH 7.2 and containing the coenzyme NADH at 4.4 mM (Sigma-Aldrich, UK). L-lactate dehydrogenase from rabbit muscle was added in quantities of 0, 40, and 80 U (Sigma-Aldrich, UK). A quantity of 1 ml of hyperpolarized pyruvate solution was added to each tube immediately before imaging to give a final pyruvate concentration of ∼4 mM. Tubes were mixed by inversion and inserted into a ^{1}H/^{13}C quadrature coil (GE Coils, Aurora, Ohio, USA), immediately followed by a 3:12 min IDEAL spiral chemical shift imaging (CSI) acquisition [31] (40 mm axial slice, TR = 500 ms, flip angle = 5, FOV = 80 mm, 40×40 points, and 4 s time resolution). Structural gradient echo ^{1}H images were obtained at the same location following the dynamic experiment (10 mm thick, 10 mm gap, 256×128, FOV = 120 mm, TR = 5.7 ms, TE = 1.7 ms, flip angle = 30).

3.1.2 | Human experiments

Brain data were previously published in Ref. [5]. Four subjects were investigated using a 3 T MR system (MR750,

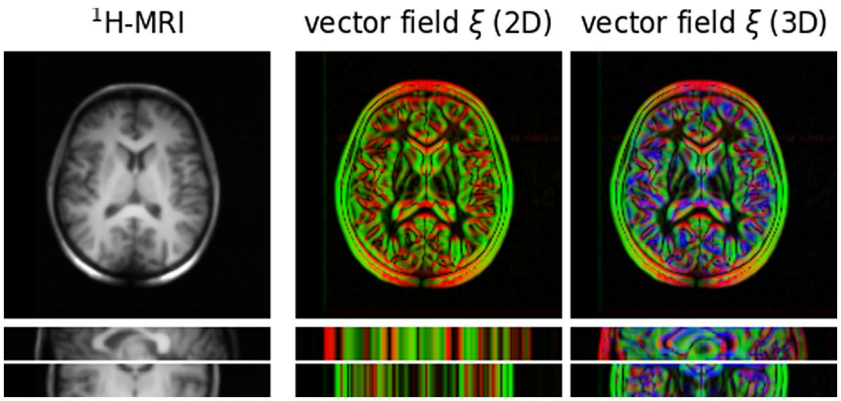

FIGURE 3 Visual representation of the vector field used in dTV. Left: ^{1}H-MRI of volunteer to be used as the *guide*. Right: modulus of vector field $\xi \in \mathbb{R}^{M\times N\times K\times 3}$ (7) with $\eta = 10^{-1}$ shown as a 3D RGB color image. Here the colors red, green, and blue correspond to the mediolateral, anteroposterior, and superoinferior directions, respectively

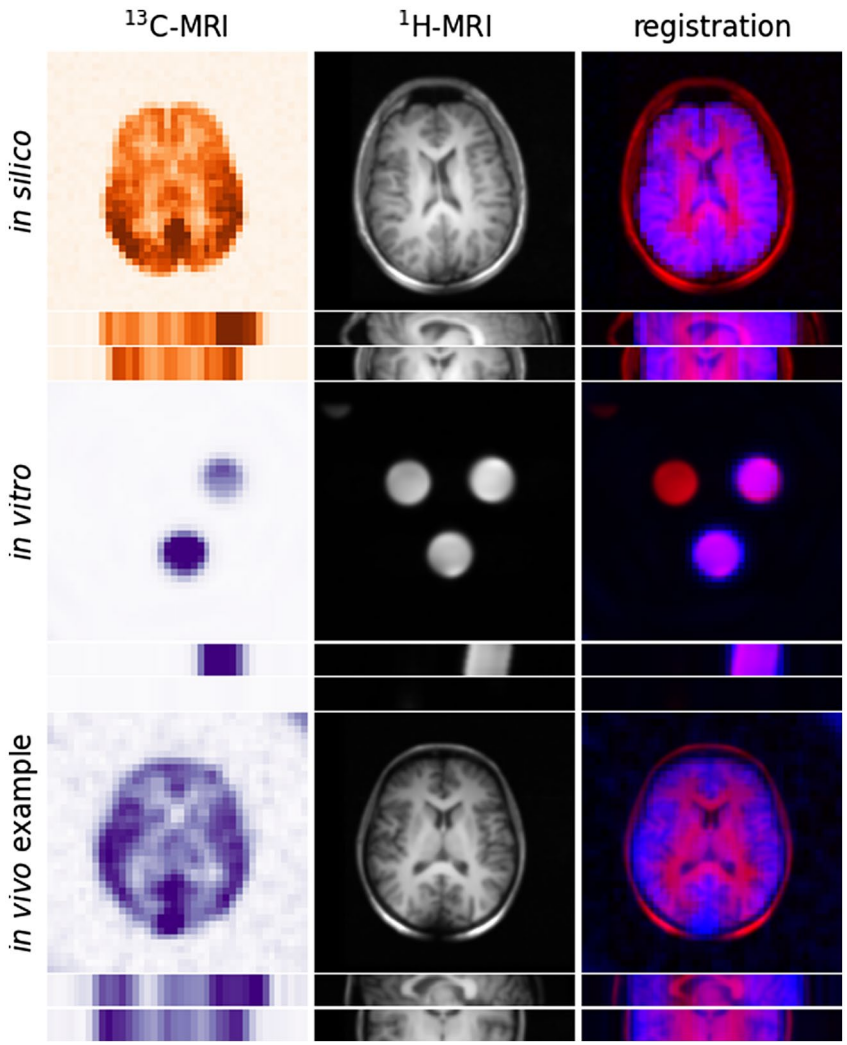

FIGURE 4 Visualization of some of the datasets used in this study. The data shown here from top to bottom is: pyruvate for the in silico data and lactate for both the in vitro and in vivo data. The alignment of the data y and the guide v is visualized as a 3D RGB image by taking v as the red channel and a scaled version of $S^T y$ as the blue channel

GE Healthcare, Waukesha WI), with a dual-tuned ^{1}H/^{13}C quadrature head coil (Rapid Biomedical, Rimpar Germany). Carbon images were acquired using IDEAL spiral imaging (flip angle = 15, FOV = 240 mm, 40×40 points, slice thickness = 30 mm, gap 3 mm) every 4 s from 10 to 70 s after the start of injection of 0.4 mL/kg of ~250 mM hyperpolarized pyruvate solution at 5 mL/s into the brachial vein. Anatomic T_1-weighted hydrogen images were acquired using a 3D inversion prepared gradient echo sequence (inversion time = 450 ms, FOV = 240 mm, TR = 8.6 ms, TE = 3.3 ms, flip angle = 12, spatial resolution = 0.9 mm × 0.9 mm × 1 mm).

3.1.3 | In silico phantom

We validate the accuracy of the proposed approach on one simulated dataset which is based on the segmentation (see paragraph below) of a T_1-weighted ^{1}H-MRI of one of the volunteers. Based on its segmentation, we assign an intensity of 9.4 to the gray matter and 2.4 to the white matter. The intensity in each compartment is multiplied by a sinosoidal wave to simulate the inhomogeneity observed in the real data. White Gaussian noise is added to the simulated data.

3.1.4 | Preprocessing

Images of pyruvate and lactate were summed over the time series. Human ^{1}H-MRI images were segmented into the gray matter, white matter, and CSF using FAST (FMRIB Software Library, Oxford, UK). The 40 and 80 U tubes in the in vitro ^{1}H-MRI image were segmented using manually defined thresholds. ^{1}H-MRI images were first smoothed by a Gaussian filter of standard deviation 0.25 pixel and then resampled to FOV = 80 mm × 80 mm × 40 mm, resolution = 0.5 mm × 0.5 mm × 10 mm for the in vitro phantom and to FOV = 240 mm × 240 mm × 30 mm, resolution = 1.5 mm × 1.5 mm × 2 mm for the in vivo data. For visualization, the aspect ratios in all figures are in accordance to their physical dimensions except for the phantom experiments where the vertical axis has been reduced by a factor of 4.

4 | RESULTS

4.1 | Comparison of methods

We compare reconstructions with dTV of ^{13}C-MRI data to a high-spatial resolution using either a slice (2D) or a volume (3D) of ^{1}H-MRI. We also compare the proposed approach with Ref. [22]. Results for the in silico phantom are shown in Figure 5. The regularization parameter α has been tuned for each method separately to minimize the mean-squared-error (MSE)

$$\mathrm{MSE}(x, x^*) = \frac{\|x - x^*\|^2}{MNK \max(x^*)}, \quad x \in \mathbb{R}^{M \times N \times K}. \tag{9}$$

The results in the top row show that a 3D reconstruction with dTV leads to anatomically better defined images compared to other approaches. In addition, the difference images in the bottom row show that the quantification is also clearly improved. Measured in terms of MSE the improvement of a 3D reconstruction with dTV compared to a 2D reconstruction with dTV and to Ref. [22] is 40% and 37%, respectively. Further results on in vivo data are shown in Figure 6 which give a similar impression as the in silico results. It can be noted that residuals ($Sx - y$) which visually mostly contain noise can only be observed for 2D-dTV for $\alpha = 5 \cdot 10^{-3}$ as well as for 3D-dTV for $\alpha = 5 \cdot 10^{-3}$ and $\alpha = 5 \cdot 10^{-2}$. This may indicate that dTV, particularly in 3D, is less in conflict with the data term and better describes the underlying anatomy. Based on these findings, we choose the largest regularization parameter which still explains the data sufficiently well which is also called Morozov's discrepancy principle, see for example, Ref. [32]. Thus, in what follows the regularization parameter for 3D-dTV has been chosen as $\alpha = 5 \cdot 10^{-2}$ for all experiments.

4.2 | Qualitative evaluation

Qualitative results of the proposed approach of the in vitro phantom and the in vivo data can be found in Figures 7 and 8. The super-resolved in vitro phantom images demonstrate well-defined edges which are consistent with the physical boundaries of the phantoms used in the study. Importantly, the high-resolution images have preserved the same contrast and signal variation as the ^{13}C-MRI data. This is confirmed by the metabolic ratio image which further highlights that the metabolic information is not being distorted.

The four cases demonstrating the in vivo results in Figure 7 also show improved resolution compared to the original data, with improved differentiation between the white and gray matter. Overall, the contrast and regional differences are largely preserved between the original data and the super-resolved images. However, consistent spatial variations remain, such as the higher signal on the

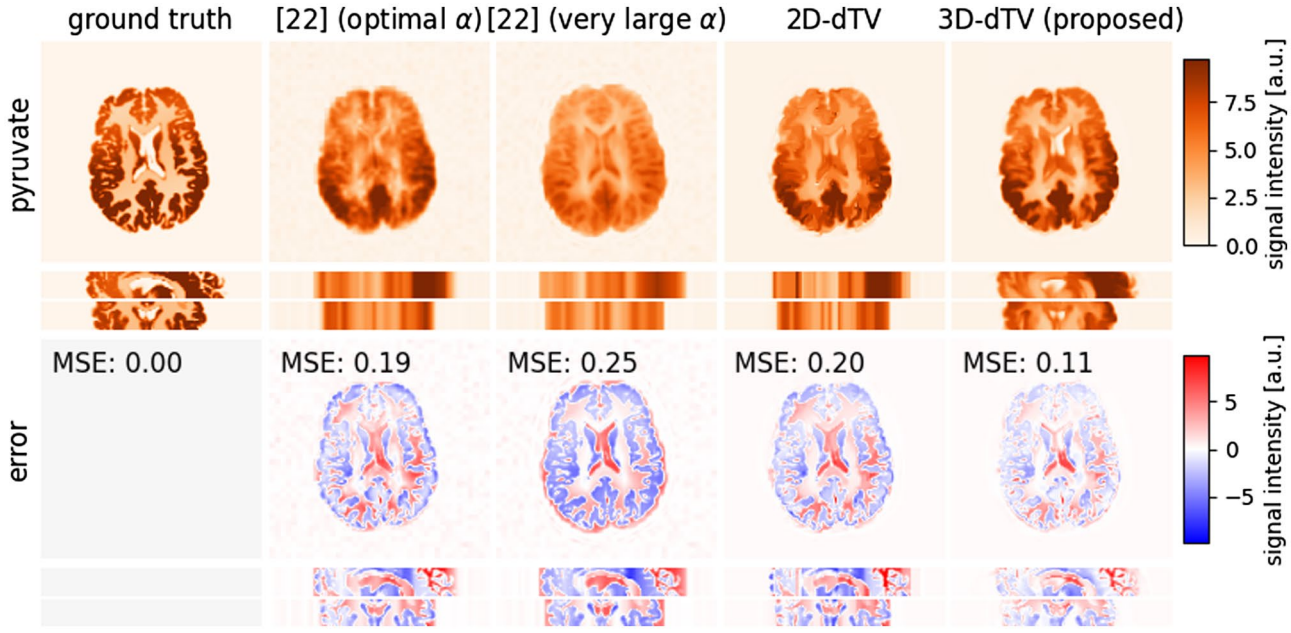

FIGURE 5 Comparison of methods showing pyruvate signal within an in silico phantom. Comparing the approach used in Ref. [22] with dTV in 2D and 3D, it can be observed that the latter leads to a better recovery of the contrast and clearer anatomical structures. Moreover, the mean-squared-error (MSE) for 3D-dTV is 37% and 40% lower compared to Ref. [22] and 2D-dTV, respectively. The anatomical assumptions in Ref. [22] can be visualized by selecting a very large regularization parameter α where gradients of the super-resolved hyperpolarized image are forced to be equal to the guide image

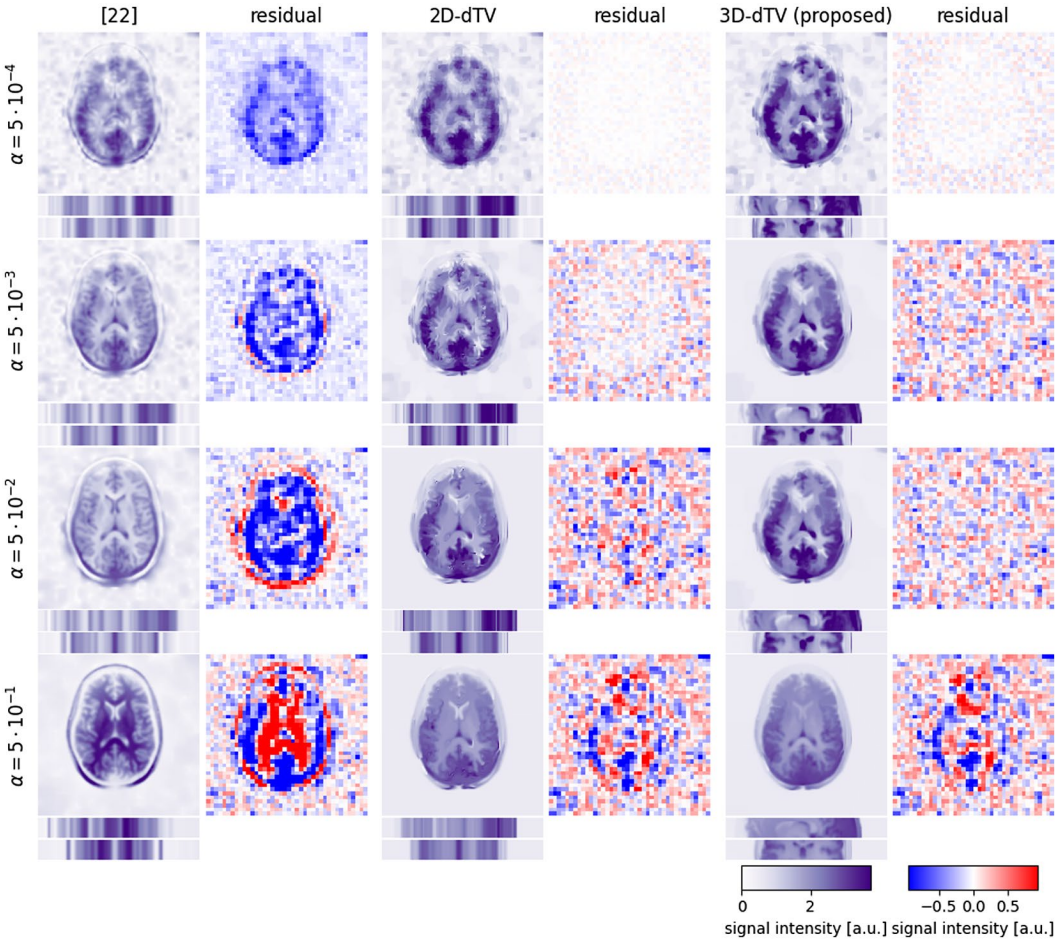

FIGURE 6 Comparison of methods showing lactate signal from the in vivo data. Similar observations as for the in silico data can be made. dTV using a 3D guide image leads to accurate discrimination of many normal brain structures, particularly in the sagittal and coronal planes, without inflation of the residual error in comparison to the other two approaches. Moreover, for large regularization parameters the method used in Ref. [22] may invert contrast between the white and gray matter

ratio images in the frontal white matter, and focal areas of high lactate and pyruvate in the gray matter in the occipital and temporal lobes. These geographic differences are often more clearly apparent on the super-resolved imaging.

Line plots across the brains (Figure 8) demonstrate the expected left–right symmetry and show that intensity variations between the gray and white matter and CSF are preserved in the super-resolution data. Tissue boundaries are neither discontinuous nor excessively smoothed. These results provide evidence that regional variations in metabolism can be more clearly ascertained during super-resolution but the contrast between areas is preserved.

4.3 | Quantitative evaluation

The proposed method is evaluated quantitatively in Figure 9 for the in vitro and in vivo data. Summary statistics for in vivo data are shown in Figure 10 and all individual data are shown in the Supporting Information. Regions of the gray matter (GM) and white matter (WM) in vivo are defined as all pixels/voxels (for 2D and 3D data, respectively) where the fuzzy segmentation exceeds 70%. For the low-resolution in vivo data, this means that statistics are computed using 60–130 pixels and for the high-resolution reconstruction around 35–59k voxels. In addition, we show a quantitative analysis of the high-resolution reconstruction using the low-resolution in order to highlight the effect of the segmentation on the conclusions. The box plots show the median (bold line), the 25% and 75% quantile (boxes) and 10% and 90% quantile (whiskers). For the in vitro phantom data, both the medians and distributions of pixel values were well maintained in the super-resolution images. In agreement with expectation, the metabolic ratio was approximately twice as high in the tube containing double the enzyme concentration. These results confirm that the super-resolved data have not significantly altered the quantitative measures of metabolism as demonstrated by comparing these in vitro

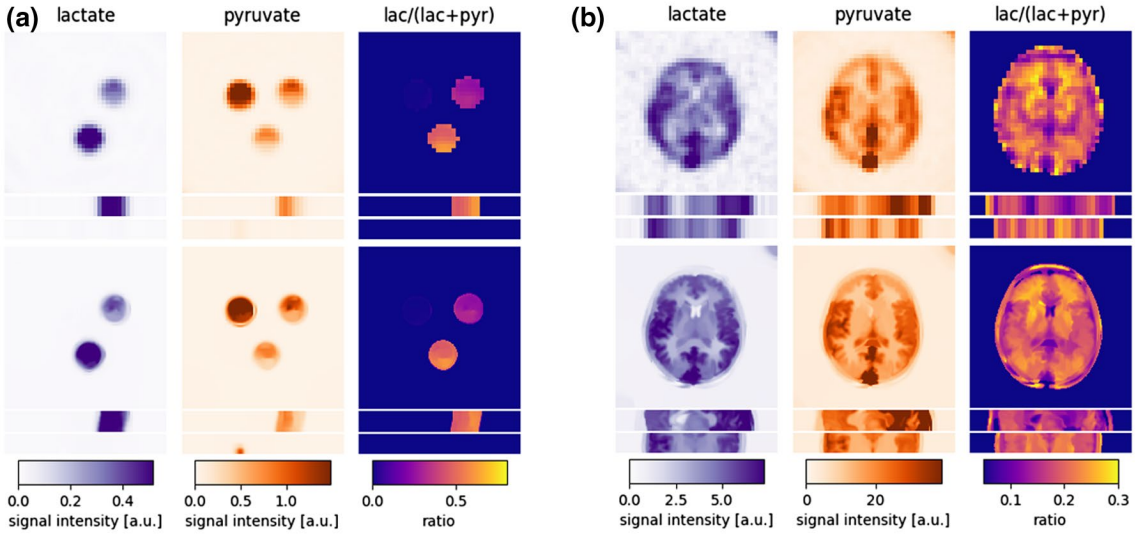

FIGURE 7 Qualitative evaluation. In both subfigures, the top row shows ^{13}C-MRI data of the metabolites lactate (lac) and pyruvate (pyr), as well as their normalized ratio. The bottom row shows super-resolved images for both metabolites and their ratio using the ^{1}H-MRI image as a guide

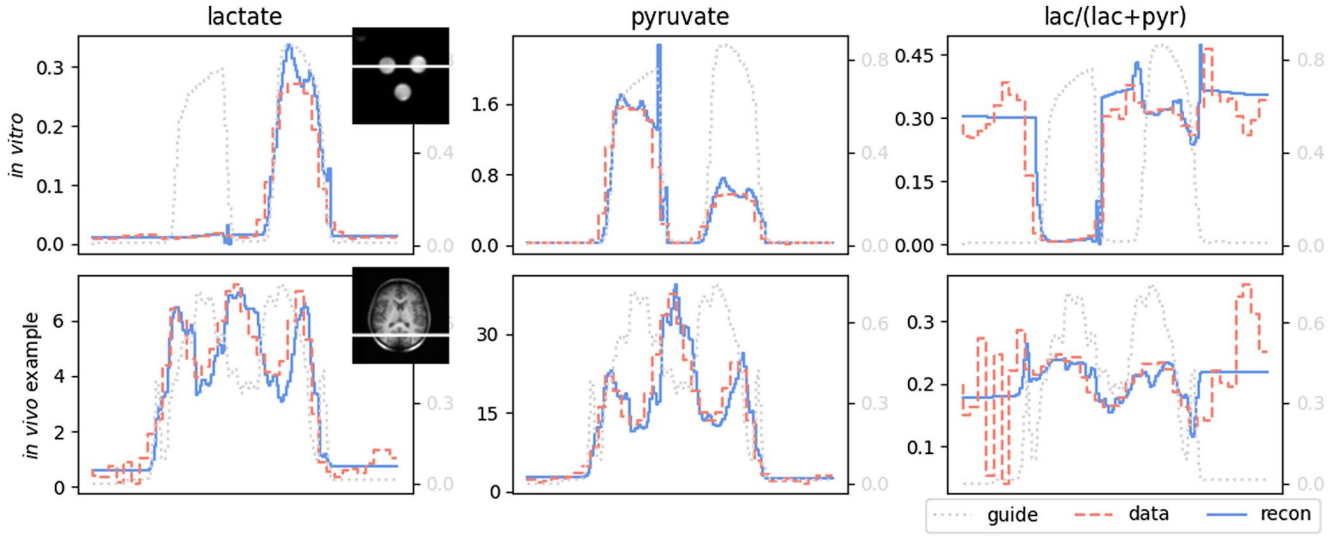

FIGURE 8 Qualitative evaluation: line profiles of images in Figure 7. A profile in vitro through the tubes containing 0 and 40 U of enzyme shows reduction of the spikes at the phantom edges caused by partial volume, while maintaining intensities within the tubes, when the super-resolution algorithm is applied. In the in vivo example, the patterns of intensity variation between tissues are maintained, without either excessively smooth or abrupt borders between them

measurements against the gold standard enzyme concentration. The quantitative values for lactate and pyruvate signal as well as the ratiometric measurements were also largely preserved in vivo. However, there was a tendency toward a slight reduction in the differences between the gray and white matter in the estimations of pyruvate and lactate following super-resolution which require future evaluation in larger studies. It can be seen that this effect is partially explained by the better segmentation which can be used for the high-resolution reconstruction. This observation is likely to reflect the inclusion of a larger percentages of pixels in the super-resolved data arising from areas of mixed tissue in the original data. Furthermore, this effect varied between cases and was most marked for the fourth in vivo dataset, see Supporting Information. As shown in Figure 10, the ratio of mean intensities in the gray and white matter is reduced by super-resolution for lactate and pyruvate but the tissue distribution of their normalized ratios is unchanged. Similar to Figure 9 this observation can largely be explained by the better segmentation of the high-resolution reconstruction.

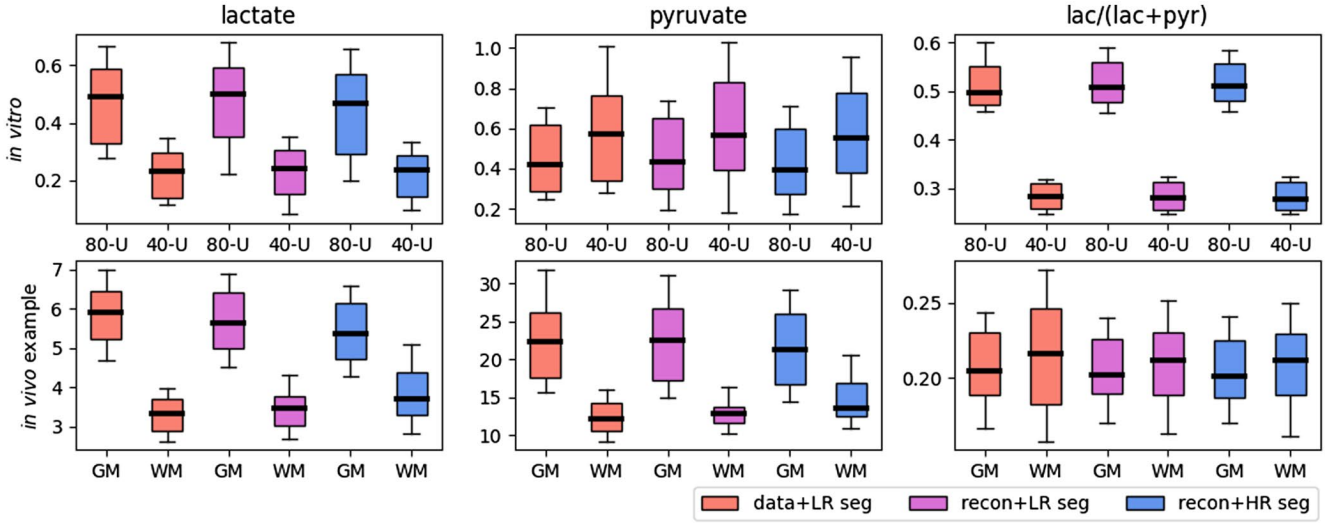

FIGURE 9 Quantitative evaluation. Statistics for lactate, pyruvate, and their normalized ratio are computed for regions of interest: 40 U and 80 U tubes for in vitro data and gray matter (GM) and white matter (WM) for an in vivo example. The plots indicate that the quantification is largely preserved through the super-resolution procedure. We highlight the influence of the segmentation by applying the low-resolution (LR) segmentation (seg) to the high-resolution (HR) reconstruction

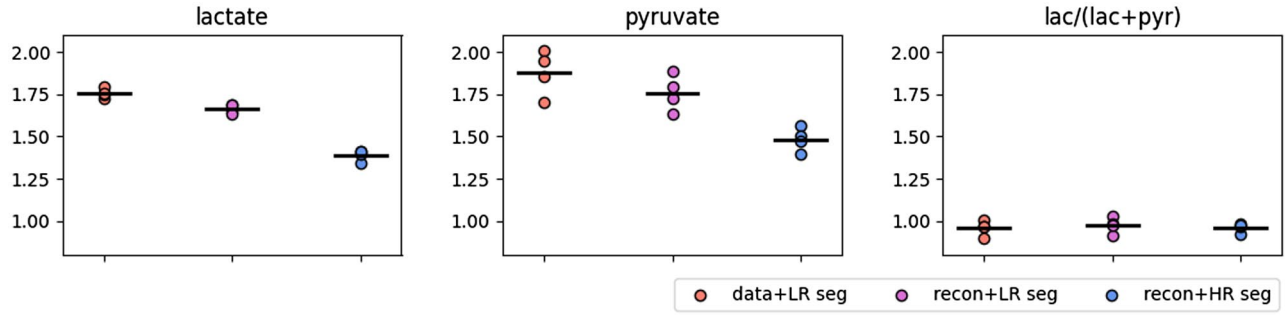

FIGURE 10 Summary statistics of in vivo data. The three subfigures show the ratio of mean intensities in the gray and white matter. Each individual dot represents the value for one of the four volunteers and the black line their mean. We highlight the influence of the segmentation by applying the low-resolution (LR) segmentation (seg) to the high-resolution (HR) reconstruction

4.4 | Computional speed

The proposed algorithm is very computational efficient. For the 3D reconstructions, it took about 0.08 s per iteration on a MacBook Pro (2.3 GHz Dual-Core Intel Core i5, 16 GB RAM) with the overall algorithm needing about 1,000 iterations, that is, 80 s. The 2D reconstructions only take 0.01 s per iteration for a similar amount of iterations.

5 | DISCUSSION

Hyperpolarized ^{13}C-MRI is an emerging technique for probing tissue metabolism in real-time. Despite the advantages of the method, overcoming low spatial resolution is one of the challenges for applying the technique more widely. The typical resolution of hyperpolarized ^{13}C-MRI is insufficient to accurately discriminate many normal anatomical brain structures that can be identified on other MRI sequences or modalities such as CT and PET. Examples within the normal brain include the boundary between the gray and white matter, the shape of the ventricles and sulci, and the location of the deep gray matter nuclei. Identification of small pathological lesions is also clinically important but difficult at low resolution. Improved spatial resolution could have implications for many aspects of clinical imaging: for example, identifying small inflammatory plaques in multiple sclerosis or small brain metastases not visible at lower resolution could have prognostic significance and could influence treatment decisions. Accurate measurements of lesion size are important for assessing treatment response and super-resolution approaches could be used to assess the effects of chemotherapy or radiotherapy. In

the field of metabolic imaging, new methods for improving resolution on PET are now used routinely on many scanners.[33,34] This paper demonstrates the potential of using 3D super-resolution techniques to enhance low resolution metabolic imaging with in silico, in vitro, and in vivo datasets.

The in vitro phantom presented here showed the power of the method to qualitatively enhance the original data while importantly maintaining the quantitative differences between the known varying enzyme concentrations in the three tubes. The in vivo data from healthy volunteers also confirmed the very significant qualitative improvement in the super-resolved images allowing anatomical regions to be more clearly discerned, such as the gray matter and the ventricles. In contrast to the in vitro data, the in vivo data showed some differences in the quantitative measurements derived from the gray and white matter following super-resolution, and this effect was variable across the four volunteers. However, unlike the phantom data, there was no gold standard to compare against and the super-resolved imaging may be more accurately representing the metabolism in these geographically distinct regions, as they may be less susceptible to partial volume effects compared to the larger voxels in the original data. In several of the subjects (e.g., in Figure 6), extracerebral metabolite signal was seen, which could have arisen from the overlying muscle and skin. The signal was too weak and inconsistent to fully characterize and may be artifactual. However, if the signal could be enhanced, with, for example, higher flip angles, the origin of this could be further explored in future studies and super-resolution may be able to better delineate these features. Applying this technique to future in vivo datasets where tissue samples are available, will allow these results to be validated against a gold standard measure of metabolism. Furthermore, super-resolved data could be used to facilitate automated segmentation of tumors or other pathological processes using the enhanced resolution that this provides, in addition to the multidimensionality of the ^{13}C-MRI data.[35]

The proposed approach depends on a couple of parameters which can be tuned for maximal performance. The most important parameters are the regularization parameter α and the two parameters for the directional total variation η and γ. Despite this, the results in this paper were achieved with minimal tuning of α and the default values for both other parameters. Once tuned, the regularization parameter can be kept constant for similar datasets (e.g., for all of the in vivo data in this paper) and still achieve very good performance.

Fluid-suppressed T1-weighted images were chosen as the input in this study due to the excellent contrast provided between the gray matter, white matter, and CSF, but the method could similarly be applied to a range of other MRI-based contrast approaches. One interesting possibility would be the injection of gadolinium-based contrast agents, to identify the blood vessels and to better characterize the vascular pool of metabolite signal. Strong signals from pyruvate and lactate are apparent in the sagittal sinus, but smaller vessels which are less well visualized in the absence of gadolinium may also have a profound effect on the measured signal, most notably pyruvate in the feeding arteries. We did not inject a contrast agent in this study of healthy controls, but these agents are frequently used in studies of patients with tumors, multiple sclerosis, or other brain lesions, so future super-resolution studies could consider the use of contrast-enhanced imaging.

The proposed framework heavily relies on the spatial alignment of the data and the guide. The required accuracy will certainly depend on the upsampling factor and further work is needed to quantify this precisely. The proposed mathematical model can be extended to estimate the resolution degradation in terms of a point-spread-function/convolution kernel[27] and to include registration,[36] both at the expense of making the optimization non-convex and therefore requiring different and computationally more expensive algorithms.

The proposed approach may be further improved by performing the super-resolution directly based on the k-space data, thereby avoiding any potential loss of information by the inversion and other postprocessing. Similar approaches are common in other imaging modalities such as PET.[9–11] This could potentially be significant if combined with compressed sensing[37] for the ^{13}C-MRI data and to handle noisier datasets, see also paragraph below.

The super-resolution of ^{13}C-MRI using ^{1}H-MRI has been undertaken using several different approaches.[22–24] Two publications have relied on segmented ^{1}H-MR images.[23,24] More broadly within MR spectroscopy, previous approaches have included combining the resolution of spectroscopic imaging with MRI using a segmentation-based compartmental model,[38,39] as well as increasing the resolution of MR spectroscopic imaging via a segmentation-based Markov random field.[13,14] It has been shown for PET partial-volume-correction[9] that relying on segmentation can decrease its robustness. In some of the previous approaches for super-resolution in ^{13}C-MRI, the authors assume that image gradients in ^{13}C-MRI and ^{1}H-MRI are identical up to a user-defined global scaling, an assumption that is most likely not met in real world applications.[22] In addition, their method is intrinsically "two-dimensional" and cannot be extended to the setting where a different number of slices are acquired for both modalities. Here we have demonstrated a direct comparison

between the proposed method and a previously published approach,[22] see also Figure 5. A key advantage of the proposed technique is that it does not rely on segmented ^{1}H-MRI and makes no unreasonable assumptions of the signal being smooth or constant in predefined anatomical regions. Observed variations are maintained both between and within the gray and white matter in different lobes of the brain.

In this paper, we studied a super-resolution approach focussing on the metabolites lactate and pyruvate which have a relatively high signal-to-noise ratio compared to other metabolites such as bicarbonate, alanine, and pyruvate hydrate. As is evident from Figure 1, the noise distribution in the reconstructed magnitude image suggests that it is intercorrelated rather than being independent and identically distributed via a Gaussian distribution, which is assumed by the proposed model. Because of the relatively high SNR, this simple image modeling did not significantly affect the reconstruction of lactate and pyruvate images. However, this simple approach is likely to negatively affect image reconstruction as the signal-to-noise level drops. In order to apply this method to metabolites with a much lower signal-to-noise ratio, high-resolution reconstruction based directly on k-space data is likely to be advantageous.

Many inverse problems are currently solved via deep neural networks, for example, see Ref. [32] and references therein. Translating these ideas is practically very challenging due to missing training data in many real world scenarios. For example in this application, we are unable to acquire high-resolution ^{13}C-MRI images needed for the training of these algorithms due to the sensitivity problem as highlighted in the introduction.

6 | CONCLUSION

We have demonstrated a method to increase the resolution of ^{13}C-MRI by using a super-resolution algorithm which makes use of an ^{1}H-MRI image routinely acquired for anatomical co-registration. Our results on a range of simulated, experimental and clinical data show that the proposed approach leads to biologically meaningful images while largely preserving the quantitative measurements of metabolism. Although the work requires clinical validation against tissue measures of metabolism, it offers great potential in the field of ^{13}C-MRI and could significantly improve image quality in the future.

ACKNOWLEDGEMENTS

We thank Dr Charlie Daniels and Dr James Grist for acquiring the in vitro and in vivo datasets.

ORCID

Matthias J. Ehrhardt https://orcid.org/0000-0001-8523-353X

TWITTER

Matthias J. Ehrhardt @MJEhrhardt

REFERENCES

1. Kurhanewicz J, Vigneron DB, Ardenkjaer-Larsen JH, et al. Hyperpolarized ^{13}C MRI: path to clinical translation in oncology. *Neoplasia (USA)*. 2019;21:1-16.
2. Ardenkjær-Larsen JH, Fridlund B, Gram A, et al. Increase in signal-to-noise ratio of >10,000 times in liquid-state NMR. *Proc Nat Acad Sci USA*. 2003;100:10158-10163.
3. Nelson SJ, Kurhanewicz J, Vigneron DB, et al. Metabolic imaging of patients with prostate cancer using hyperpolarized [1-13C]pyruvate. *Sci Trans Med*. 2013;5.
4. Zaccagna F, Grist JT, Deen SS, et al. Hyperpolarized Carbon-13 magnetic resonance spectroscopic imaging: a clinical tool for studying tumour metabolism. *Br J Radiol*. 2018;91:1-11.
5. Grist JT, McLean MA, Riemer F, et al. Quantifying normal human brain metabolism using hyperpolarized [1-13C] pyruvate and magnetic resonance imaging. *NeuroImage*. 2019;189:171-179.
6. Grist JT, Miller JJ, Zaccagna F, et al. Hyperpolarized ^{13}C MRI: a novel approach for probing cerebral metabolism in health and neurological disease. *J Cereb Blood Flow Metabo*. 2020;40:1137-1147.
7. Woitek R, Gallagher F. The use of hyperpolarised ^{13}C MRI in clinical body imaging to probe cancer metabolism. *Br J Cancer*. 2020.
8. Lee CY, Soliman H, Geraghty BJ, et al. Lactate topography of the human brain using hyperpolarized ^{13}C-MRI. *NeuroImage*. 2020;204:116202.
9. Vunckx K, Atre A, Baete K, et al. Evaluation of three MRI-based anatomical priors for quantitative PET brain imaging. *IEEE Trans Med Imaging*. 2012;31:599-612.
10. Schramm G, Holler M, Rezaei A, et al. Evaluation of parallel level sets and Bowsher's method as segmentation-free anatomical priors for time-of-flight PET reconstruction. *IEEE Trans Med Imaging*. 2017;37:590-603.
11. Ehrhardt MJ, Markiewicz PJ, Liljeroth M, et al. PET reconstruction with an anatomical MRI prior using parallel level sets. *IEEE Trans Med Imaging*. 2016;35:2189-2199.
12. Teh I, Mcclymont D, Carruth E, Omens J, Mcculloch A, Schneider JE. Improved compressed sensing and super-resolution of cardiac diffusion MRI with structure-guided total variation. *Magn Reson Med*. 2020;84:1868-1880.
13. Haldar JP, Hernando D, Song SK, Liang ZP. Anatomically constrained reconstruction from noisy data. *Magn Reson Med*. 2008;59:810-818.
14. Kornak J, Young K, Soher BJ, Maudsley AA. Bayesian κ-space time reconstruction of MR spectroscopic imaging for enhanced resolution. *IEEE Trans Med Imaging*. 2010;29:1333-1350.
15. Gnahm C, Bock M, Bachert P, Semmler W, Behl NG, Nagel AM. Iterative 3D projection reconstruction of ^{23}Na data with an ^{1}H MRI constraint. *Magn Reson Med*. 2014;71:1720-1732.

16. Obert AJ, Gutberlet M, Kern AL, et al. ^{1}H-guided reconstruction of 19F gas MRI in COPD patients. *Magn Reson Med*. 2020;84:1336-1346.
17. Manjón JV, Coupé P, Buades A, Collins DL, Robles M. MRI superresolution using self-similarity and image priors. *Int J Biomed Imaging*. 2010;2010:1-11.
18. Bilgic B, Goyal VK, Adalsteinsson E. Multi-contrast reconstruction with Bayesian compressed sensing. *Magn Reson Med*. 2011;66:1601-1615.
19. Ehrhardt MJ, Betcke MM. Multi-contrast MRI reconstruction with structure-guided total variation. *SIAM J Imaging Sci*. 2016;9:1084-1106.
20. Zhu Q, Ren Y, Qiu Z, Wang W. Robust MR image super-resolution reconstruction with cross-modal edge-preserving regularization. *Int J Imaging Syst Technol*. 2019;29:491-500.
21. Rasch J, Kolehmainen V, Nivajarvi R, et al. Dynamic MRI reconstruction from undersampled data with an anatomical prescan. *Inverse Prob*. 2018;34.
22. Dwork N, Gordon JW, Tang S, et al. Di-chromatic interpolation of magnetic resonance metabolic images. *Magn Reson Mater Phys Biol Med*. 2021;34:57-72.
23. Farkash G, Markovic S, Novakovic M, Frydman L. Enhanced hyperpolarized chemical shift imaging based on a priori segmented information. *Magn Reson Med*. 2019;81:3080-3093.
24. Ma J, Park JM. Super-resolution hyperpolarized ^{13}C imaging of human brain using patch-based algorithm. *Tomography*. 2020;6:343-355.
25. Ehrhardt M J. Multi-modality imaging with structure-promoting regularizers. In: Younces L, ed. *Handbook of Mathematical Models and Algorithms in Computer Vision and Imaging*; 2021:1-38.
26. Chambolle A, Pock T. A first-order primal-dual algorithm for convex problems with applications to imaging. *J Math Imaging Vision*. 2011;40:120-145.
27. Bungert L, Coomes DA, Ehrhardt MJ, Rasch J, Reisenhofer R, Schönlieb C-B. Blind image fusion for hyperspectral imaging with the directional total variation. *Inverse Prob*. 2018;34:044003.
28. Chambolle A, Pock T. An introduction to continuous optimization for imaging. *Acta Numerica*. 2016;25:161-319.
29. Adler J, Kohr H, Öktem O. Online. *Oper Discretization Library*. 2017. https://doi.org/10.5281/zenodo.249479
30. Daniels CJ, Mclean MA, Schulte RF, et al. A comparison of quantitative methods for clinical imaging with hyperpolarized ^{13}C-pyruvate. *NMR Biomed*. 2016;29:387-399.
31. Wiesinger F, Weidl E, Menzel MI, et al. IDEAL spiral CSI for dynamic metabolic MR imaging of hyperpolarized [1-13C]pyruvate. *Magn Reson Med*. 2012;68:8-16.
32. Arridge S, Maass P, Öktem O, Schönlieb C-B. Solving inverse problems using data-driven models. *Acta Numerica*. 2019;28:1-174.
33. Teoh EJ, McGowan DR, Macpherson RE, Bradley KM, Gleeson FV. Phantom and clinical evaluation of the Bayesian penalized likelihood reconstruction algorithm Q.Clear on an LYSO PET/CT System28880161. *J Nucl Med*. 2015;56:1447-1452.
34. Wu Z, Guo B, Huang B, et al. Phantom and clinical assessment of small pulmonary nodules using Q.Clear reconstruction on a silicon-photomultiplier-based time-of-flight PET/CT system. *Sci Rep*. 2021;11:1-9.
35. Daniels CJ, Gallagher FA. Unsupervised segmentation of 5D Hyperpolarized Carbon-13 MRI data using a fuzzy Markov random field model. *IEEE Trans Med Imaging*. 2018;37:840-850.
36. Bungert L, Ehrhardt MJ. Robust image reconstruction with misaligned structural information. *IEEE Access*. 2020;8:222944-222955.
37. Lustig M, Donoho DL, Pauly JM. Sparse MRI: the application of compressed sensing for rapid MR imaging. *Magn Reson Med*. 2007;58:1182-1195.
38. Hu X, Levin DN, Lauterbur PC, Spraggins T. SLIM: Spectral localization by imaging. *Magn Reson Med*. 1988;8:314-322.
39. Liang Z-P, Lauterbur PC. A Generalized Series Approach to MR Spectroscopic Imaging. *IEEE Trans Med Imaging*. 1991;10:132-137.

SUPPORTING INFORMATION

Additional supporting information may be found in the online version of the article at the publisher's website.

FIGURE S1 Qualitative evaluation. In each subfigure, the top row shows ^{13}C-MRI data of two metabolites lactate (lac) and pyruvate (pyr) as well as their normalized ratio. The bottom row shows super-resolved images for both metabolites as well as their ratio using the ^{1}H-MRI image as a guide. This figure is an extended version of figure 7 in the main paper, showing data from all 4 volunteers

FIGURE S2 Qualitative evaluation: Line profiles of images in figure S1. For the in vitro data, a profile through the tubes containing 0 U and 40 U of enzyme shows reduction of the spikes at the phantom edges caused by partial volume, while maintaining intensities within the tubes. In all subjects the patterns of intensity variation between tissues are maintained, without either excessively smooth or abrupt borders between them. This figure is an extended version of figure 8 in the main paper

FIGURE S3 Quantitative evaluation. Statistics for lactate, pyruvate, and their normalized ratio are computed for regions of interest: 40 U and 80 U tubes for in vitro data and gray matter (GM) and white matter (WM) for in vivo data. The plots indicate that the quantification is largely preserved through the super-resolution procedure. This figure is an extended version of figure 9 in the main paper. We highlight the in uence of the segmentation by applying the low-resolution (LR) segmentation (seg) to the high-resolution (HR) reconstruction

How to cite this article: Ehrhardt MJ, Gallagher FA, McLean MA, Schönlieb C-B. Enhancing the spatial resolution of hyperpolarized carbon-13 MRI of human brain metabolism using structure guidance. *Magn Reson Med*. 2021;00:1–12. doi:10.1002/mrm.29045